jove

Co-localizing Kelvin Probe Force Microscopy with Other Microscopies and Spectroscopies: Selected Applications in Corrosion Characterization of Alloys

Olivia O. Maryon[*,1], **Corey M. Efaw**[*,1], **Frank W. DelRio**[2], **Elton Graugnard**[1,3], **Michael F. Hurley**[1,3], **Paul H. Davis**[1,3]

[1] Micron School of Materials Science & Engineering, Boise State University [2] Material, Physical, and Chemical Sciences Center, Sandia National Laboratories [3] Center for Advanced Energy Studies

[*] These authors contributed equally

Corresponding Author

Paul H. Davis
pauldavis2@boisestate.edu

Citation

Maryon, O.O., Efaw, C.M., DelRio, F.W., Graugnard, E., Hurley, M.F., Davis, P.H. Co-localizing Kelvin Probe Force Microscopy with Other Microscopies and Spectroscopies: Selected Applications in Corrosion Characterization of Alloys. *J. Vis. Exp.* (184), e64102, doi:10.3791/64102 (2022).

Date Published

June 27, 2022

DOI

10.3791/64102

URL

jove.com/video/64102

Abstract

Kelvin probe force microscopy (KPFM), sometimes referred to as surface potential microscopy, is the nanoscale version of the venerable scanning Kelvin probe, both of which measure the Volta potential difference (VPD) between an oscillating probe tip and a sample surface by applying a nulling voltage equal in magnitude but opposite in sign to the tip-sample potential difference. By scanning a conductive KPFM probe over a sample surface, nanoscale variations in surface topography and potential can be mapped, identifying likely anodic and cathodic regions, as well as quantifying the inherent material driving force for galvanic corrosion.

Subsequent co-localization of KPFM Volta potential maps with advanced scanning electron microscopy (SEM) techniques, including back scattered electron (BSE) images, energy dispersive spectroscopy (EDS) elemental composition maps, and electron backscattered diffraction (EBSD) inverse pole figures can provide further insight into structure-property-performance relationships. Here, the results of several studies co-localizing KPFM with SEM on a wide variety of alloys of technological interest are presented, demonstrating the utility of combining these techniques at the nanoscale to elucidate corrosion initiation and propagation.

Important points to consider and potential pitfalls to avoid in such investigations are also highlighted: in particular, probe calibration and the potential confounding effects on the measured VPDs of the testing environment and sample surface, including ambient humidity (i.e., adsorbed water), surface reactions/oxidation, and polishing debris or other contaminants. Additionally, an example is provided of co-localizing a third technique, scanning confocal Raman microscopy, to demonstrate the general

applicability and utility of the co-localization method to provide further structural insight beyond that afforded by electron microscopy-based techniques.

Introduction

Microscopic characterization of materials is fundamentally important for understanding and developing new materials. Numerous microscopy methods provide maps of material surfaces and their properties, including topography, elasticity, strain, electrical and thermal conductivity, surface potential, elemental composition, and crystal orientation. However, the information provided by one microscopy modality is often insufficient to fully understand the collection of properties that may be contributing to the material behavior of interest. In some cases, advanced microscopes have been constructed with combined characterization capabilities, such as an inverted optical microscope platform that incorporates an atomic force microscope (AFM) or utilizing multiple scanning probe modalities (e.g., Kelvin probe force microscopy [KPFM] or intermodulation electrostatic force microscopy [ImEFM[1]], surface potential measurements, and magnetic force microscopy [MFM])[2,3,4,5] to characterize a sample on the same AFM. More generally, one would like to combine the information from two separate microscopes to obtain structure-property correlations[6,7]. The co-localization of scanning Kelvin probe force microscopy with scanning electron and Raman-based microscopies and spectroscopies is presented here to illustrate a process for correlating information obtained from two or more separate microscopes by way of a specific application example, namely, multi-modal characterization of metal alloys to understand corrosion behavior.

Corrosion is the process by which materials react chemically and electrochemically with their environment[8]. Electrochemical corrosion is a spontaneous (i.e., thermodynamically favorable, driven by a net decrease in free energy) process involving electron and charge transfer that occurs between an anode and a cathode in the presence of an electrolyte. When corrosion occurs on a metal or alloy surface, anodic and cathodic regions develop based on variations in the composition of microstructural features in a process known as micro-galvanic corrosion[9]. Through the use of co-localized, nanoscale characterization techniques, the methods described here provide an experimental route to identify likely micro-galvanic couples between a wide variety of alloy microstructural features, providing potentially helpful insight for corrosion mitigation and the development of new materials. The results of these experiments can determine which microstructural features at the alloy surface are likely to serve as local anode sites (i.e., sites of oxidation) or cathodes (i.e., sites of reduction) during active corrosion, as well as provide new insight into the nanoscale features of corrosion initiation and reactions.

KPFM is an AFM-based scanning probe microscopy (SPM) characterization technique that can generate simultaneous (or line-by-line sequential) topography and Volta potential difference (VPD) maps of a sample surface with resolutions in the order of 10 nanometers and millivolts, respectively[10]. To accomplish this, KPFM utilizes a conductive AFM probe with a nanoscale tip. Typically, the probe first tracks the topographical variations in the sample surface, then lifts to a user-defined height above the sample surface before retracing the topography line to measure the VPD

between the probe and the sample (i.e., the relative Volta potential of the sample surface). Although there are multiple ways of practically implementing KPFM measurements, fundamentally, the determination of the VPD is carried out by simultaneously applying both an AC bias (in the presented implementation, to the probe) and a variable DC bias (in the presented implementation, to the sample) to null the tip-sample potential difference as indicated by nulling the oscillation of the probe at the applied AC bias frequency (or its heterodyne-amplified sum and difference frequencies on either side of the probe's natural mechanical resonance frequency) [11]. Regardless of the implementation method, KPFM produces correlated high lateral spatial resolution topography and VPD maps across a metallic surface[12].

The VPD measured via KPFM is directly correlated to the difference in work function between the sample and probe, and furthermore, the VPD (generally) trends with the electrode potential in solution[13,14,15]. This relationship can be used to determine the expected (local) electrode behavior of microstructural features based on the VPD and has been explored for a number of metal alloy corroding systems[15,16,17,18,19,20,21,22]. Additionally, the measured VPD is sensitive to local composition, surface layers, and grain/crystal/defect structure, and, hence, provides nanoscale elucidation of the features that are expected to initiate and drive corrosion reactions on a metal surface. It should be noted that the VPD (Ψ) is related to, but distinct from, the (non-measurable) surface potential (χ), as described in greater detail in the literature[13,14], including helpful diagrams and precise definitions of correct electrochemistry terminology[23]. Recent advancements in the application of KPFM to corrosion studies have greatly increased the quality and repeatability of acquired data through careful consideration of the influence of sample preparation, measurement parameters, probe type, and external environment[24,25,26,27].

One drawback of KPFM is that, while it generates a nanoscale resolution map of the surface VPD, it provides no direct information regarding composition, and, thus, the correlation of variations in VPD to differences in elemental composition must be provided by co-localization with complementary characterization techniques. By co-localizing KPFM with SEM, energy dispersive spectroscopy (EDS), electron backscattered diffraction (EBSD), and/or Raman spectroscopy, such compositional and/or structural information can be determined. However, co-localizing nanoscale techniques can be difficult due to the extreme magnification of the imaging, differences in field of view and resolution, and sample interactions during characterization[28]. Obtaining nano- to microscale images of the same region of a sample on different instruments requires high precision and careful planning to co-localize techniques and minimize artifacts due to possible cross-contamination during sequential characterization[18,28].

The aim of this article is to define a systematic method for co-localizing KPFM and SEM imaging, the latter of which can be substituted for by other characterization techniques such as EDS, EBSD, or Raman spectroscopy. It is necessary to understand the proper ordering of characterization steps, the environmental effects on KPFM resolution and measured VPDs, KPFM probe calibration, and various strategies that can be employed to successfully co-localize SEM or other advanced microscopy and spectroscopy techniques with KPFM. Accordingly, a step-by-step generalized procedure for co-localizing SEM with KPFM is provided, followed by exemplary works of such co-localization along with helpful tips and tricks to obtain meaningful results. More generally,

the procedure described here should serve to outline a broadly applicable process for co-localizing images/property maps obtained from other microscopy modalities with KPFM and other AFM modes to obtain useful structure-property relationships in a variety of material systems[6,7,29,30,31,32].

Protocol

1. Example sample preparation for co-localized imaging of a metal alloy

1. Prepare samples that are small enough to meet the dimensional requirements of the AFM and other characterization tools to be employed (e.g., in the case of the AFM used here, see the **Table of Materials**, ensure the samples have a height <18 mm to fit under the AFM head), are smooth enough on the bottom to seal against the AFM stage's sample chuck vacuum, exhibit minimal surface roughness with no loose debris, and provide a conductive path from the base to the top surface.
    1. Cut the samples to acceptable dimensions and embed in high vacuum compatible epoxy (see the **Table of Materials**; a ~25 mm diameter cylindrical mold is typical).
2. Polish the samples to nanometer-scale surface roughness.
    NOTE: A representative polishing method is provided; see references herein for alternative polishing methods employed for specific materials or samples. The example polishing method below employs hand polishing using a polishing wheel.
    1. Start with coarser grits and progressively work toward finer grit silicon carbide abrasive discs.
        1. Work from coarse to fine grit (e.g., ANSI Standard 120 grit to 1200 grit) silicon carbide abrasive discs, spending 5 min at each grit level. Between each grit level, check the sample under an optical microscope to visually confirm minimal to no scratches.
            NOTE: ANSI Standard 120 grit and 1200 grit abrasive papers correspond to European P-Grade P120 and P4000, respectively.
    2. Hand polish for 10 min using a non-aqueous 1 µm diamond suspension, followed by a 0.05 µm diamond suspension.
    3. Using a vibratory polisher, polish the sample for 24 h with 0.05 µm or 0.08 µm aqueous colloidal silica polish.
        NOTE: Using a vibratory polisher allows for a finer finish than hand polishing and will result in higher-quality KPFM images.
    4. If the material under study does not undergo rapid oxidation, rinse the sample with deionized water (or another appropriate, less-oxidizing solvent such as an anhydrous alcohol) before sonicating in a beaker with an appropriate solvent (e.g., ethanol, depending upon epoxy and polishing compounds used, as well as alloy composition) to remove any residual polishing compound or material debris.
    5. Remove the sample from the sonicator, rinse with solvent, and dry with compressed air or ultrahigh purity (UHP, 99.999%) compressed nitrogen gas.
    6. Use optical microscopy to determine if the polish is sufficient. Ensure that the sample has virtually no visible scratches on the surface (ideally appears mirror-like).

3. Implement the desired co-localization method to create an origin and axes (i.e., sample location/registration and orientation/rotation).

   NOTE: Possible co-localization methods include a nanoindent array, scratch fiducial, indelible ink dot, or other feature easily recognizable in the optical systems of the microscopes to be co-localized. See **Figure 1** for an example of easily recognizable optical features visible after polishing.

1. Perform nanoindention before or after polishing using a commercial instrumented nanoindenter to produce recognizable fiducial markers (**Figure 2**).
2. Alternatively, make ink dots or scratches (e.g., with a micromanipulator probe, razor blade, or diamond scribe) after polishing. If corrosion testing is to be performed on the sample later, avoid these methods.

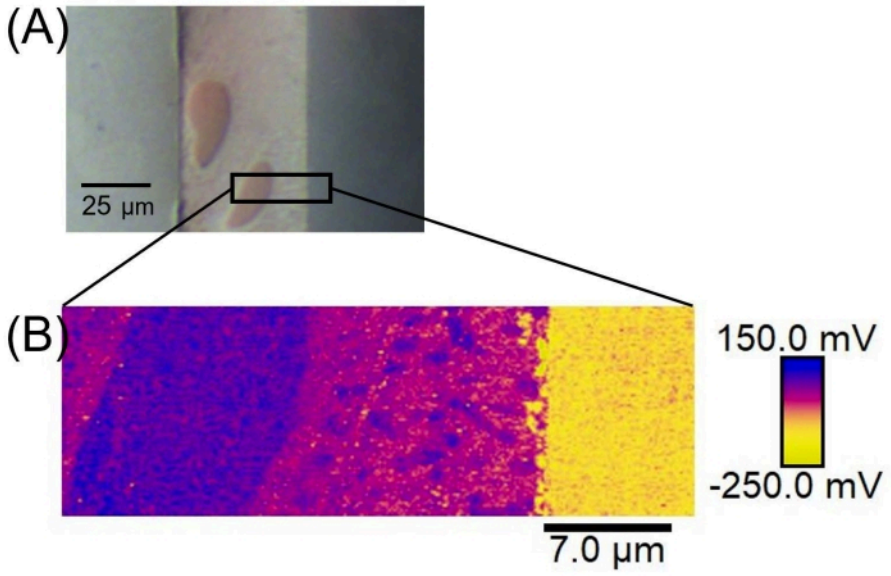

Figure 1: Co-localized optical microscope and KPFM images. (**A**) Optical microscope and (**B**) zoomed KPFM image of the boxed region in **A** of a Cu-Ag-Ti (CuSil) braze showing clear evidence of copper-rich and silver-rich phase-separated domains within the braze alloy, distinct enough to be identified by eye[30]. Scale bars: (**A**) 25 µm, (**B**) 7 µm. Abbreviation: KPFM = Kelvin probe force microscopy. Please click here to view a larger version of this figure.

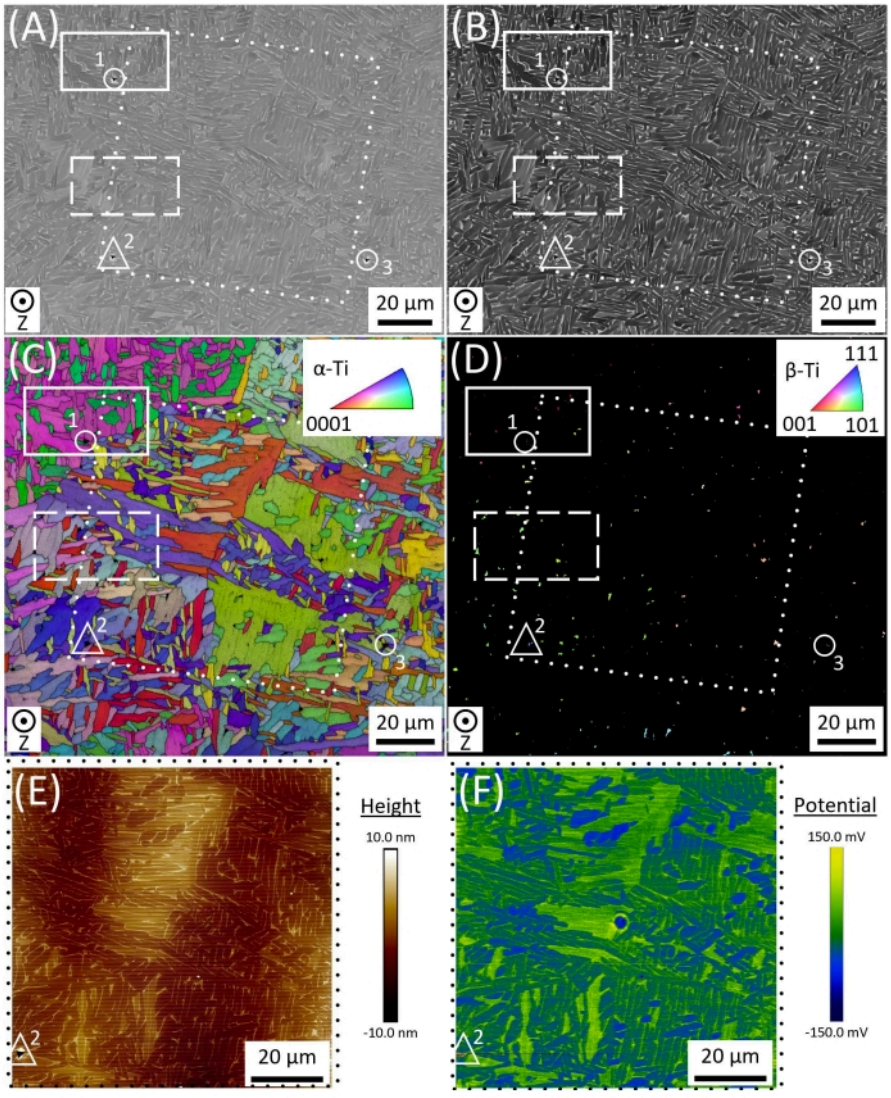

Figure 2: Nanoindentation fiducials for co-localization of KPFM and electron microscopy. Creation of an asymmetric pattern of three fiducial marks (labeled 1-3 and indicated by two circles for the XY axes and a triangle for the origin) by a nanoindenter equipped with a diamond Berkovich probe allowed for analysis of the same region of interest using multiple characterization techniques: (**A**) SE SEM imaging, (**B**) BSE SEM imaging, and EBSD measurements of (**C**) *α*-Ti and (**D**) *β*-Ti. The area indicated by the tilted, dotted square in panels **A–D** was subsequently characterized with AFM/KPFM to produce (**E**) height and (**F**) Volta potential images. The small solid and dashed rectangles in **A–D** represent areas of higher resolution KPFM scans analyzed in greater detail (see **Figure 9**). This figure is reproduced from Benzing et al.[32]. Scale bars = 20 µm. Abbreviations: KPFM = Kelvin probe force microscopy; SE = secondary electron; SEM = scanning electron microscopy; BSE = back scattered electron; EBSD = electron backscattered diffraction; AFM = atomic force microscopy. Please click here to view a larger version of this figure.

2. KPFM imaging

1. Turn on the AFM and open the corresponding control software (specific to the AFM, see the **Table of Materials** and KPFM standard operating procedure (SOP) included in the **Supplementary Materials**). In the **Select Experiment** window that opens, select the appropriate **Experiment Category, Experiment Group**, and **Experiment** (**Electrical & Magnetic, Electrical & Magnetic Lift Modes**, and **PeakForce KPFM** in this case; see **Figure 1** in **Supplementary Materials** SOP), then click **Load Experiment** to open the desired workflow. Once the experiment workflow has opened, click on **Setup** in the workflow.
2. Mount and secure a conductive AFM probe on the appropriate probe holder (see the **Table of Materials**), install the probe holder on the AFM head, and align the laser onto the back of the probe cantilever and into the position-sensitive detector (PSD). (See SOP in **Supplementary Materials** for more details and images of the probe loading and laser alignment procedures).
   NOTE: Ensure that the probe holder chosen provides a continuous electrical path from the probe to the AFM for biasing.
   1. Carefully load the probe onto the probe holder. Remove the AFM head. Install the probe and probe holder by aligning the holes on the probe holder with the contact pins on the head. Reinstall the head on the AFM and secure the head in place.
      NOTE: Electrostatic discharge (ESD) can easily damage the conductive metal coating on many KPFM probes as well as sensitive AFM electronics, so depending on the environmental conditions (e.g., humidity), consider countermeasures such as wearing anti-ESD gloves and/or using a grounding wrist strap or mat.
   2. In the **Probe Setup** menu, ensure the **Probe Type** being used is displayed. If necessary, click **Select Probe** and choose the correct probe type from the dropdown menu, then click **Return and Save Changes**.
   3. In the **Focus Tip** menu, bring the end of the cantilever into focus using the **Focus Controls** up/down arrows. Adjust the focus **Speed**, optical **Zoom**, and video **Illumination** as needed. Once the end of the cantilever is in focus, align the crosshair over the tip location by clicking on the optical image at the location corresponding to the tip's position beneath the cantilever based on the known setback of the tip from the distal end of the cantilever.
      NOTE: The tip setback is typically specified by/available from the probe manufacturer.
   4. Using the **Laser Alignment** knobs on the AFM head, align the laser onto the center of the back of the probe cantilever toward the distal end (i.e., toward the tip/away from the probe substrate) and center the reflected beam on the PSD to maximize the **Sum** voltage while minimizing the **Vertical** and **Horizontal** deflections.
3. Load the sample on the chuck and turn on the **Chuck Vacuum** using the **On/Off** lever switch. Apply a thin line of conductive silver paste (see the **Table of Materials**) to provide a continuous electrical path from the sample to the chuck. Once the silver paste has dried, check to ensure the top surface of the sample has good continuity to the sample chuck/stage using a multimeter. (See SOP in **Supplementary Materials** for more details.)

NOTE: If the electrical connection between the sample and the stage/chuck is not good, the potential channel data obtained during KPFM imaging will be noisy and/or erroneous.

4. Select the **Navigate** window in the AFM control software workflow and move the probe over the sample using the stage movement **XY Control** arrows. Bring the sample surface into focus using the **Scan Head** up/down arrows, then use the stage movement **XY Control** arrows again to locate the designated origin and move to the region of interest (ROI). (See **Figure 8** and **Figure 9** in the **Supplementary Materials** SOP).

    1. Approach the surface cautiously (adjust the scan head movement speed as needed) and bring the surface into focus. Be careful not to crash the probe into the sample surface, as this could result in probe or sample damage.

        NOTE: The AFM control software used here provides two focusing options: **Sample (default)** and **Tip Reflection**. The former employs a 1 mm focal length such that the AFM cantilever will be ~1 mm above the surface when the surface appears in focus in the optical view. The latter employs a 2 mm focal length such that the surface will appear in focus when the AFM cantilever is ~2 mm above the surface, while the tip reflection will appear in focus when the cantilever is ~1 mm above the surface (assuming a highly polished, reflective sample surface). Thus, a suggested method of approaching the surface is to begin in **Tip Reflection** mode and approach at full speed (100%) until the sample surface comes into focus, then switch to **Sample (default)** and approach at medium speed (20%) to go from 2 mm to 1 mm above the surface.

    2. Use the stage movement **XY Control** to position an easily identifiable/distinctive feature directly beneath the probe tip (indicated by the crosshair in the optical viewing window for the AFM and software used here). Once over the feature, correct for the parallax induced by the side-mounted camera optics by clicking **Calibrate** in the toolbar, then selecting **Optical** and **Optics/SPM Axis Co-linearity**. Walk through the co-linearity calibration steps by clicking **Next**. Align the crosshairs over the same distinctive feature in each of the presented optical images before clicking **Finish**, then click **Navigate** in the software workflow to continue.

    3. Locate the designated origin (based on the co-localization method chosen/used) and align the X and Y coordinate axes (i.e., sample orientation and rotation) accordingly, centering the probe tip over the origin. To enable repeatable navigation to the desired ROI and co-localization with other characterization techniques/instruments, note the X and Y position values (in µm) shown at the bottom of the software window. Once over the designated origin, record the XY position, then move to the desired area (ROI) and record the new XY position. Calculate the difference between these two locations to determine the distance to move in the X and Y directions when co-localizing KPFM with other microscopy and spectroscopy techniques.

        NOTE: There are multiple ways to determine and define the location of the ROI relative to the origin, as described in greater detail in the sub-steps below.

        1. Click **Stage** in the toolbar and select **Move To**. Record the origin XY position and then input either absolute (default) or relative (by selecting

the **Relative Motion** checkbox) X and Y move values based on the desired distance from the origin for the ROI (or navigate to the ROI using the stage movement controls and note the new XY position).

2. Alternatively, the most intuitive and, hence, preferred method is to click **Stage** in the toolbar and select **Set References**. While over the designated origin, click **Mark Point as Origin** under **Define Origin** to zero the X and Y location values. Then, move the probe to the desired ROI and note the distance from the origin to the ROI displayed as the X and Y values at the bottom of the screen.

5. Close and lock the acoustic hood enclosing the AFM.
NOTE: The above method assumes a standard ambient environment AFM system, but KPFM can also be performed in an inert atmosphere glovebox. While more challenging, employing an AFM housed in a glovebox can be highly beneficial due to reduced amounts of surface water, as it enables lower lift heights (and hence, higher spatial resolution) and more reproducible VPD measurements relative to the variable humidity experienced in ambient conditions, as well as preventing passive oxide layer formation or corrosion on the sample after polishing (**Figure 3**). If conducting KPFM experiments under ambient conditions, it is advisable to carefully control (if possible) and monitor the temperature and relative humidity. See the discussion for more detail.

6. Select the **Check Parameters** workflow window and ensure the default initial imaging parameters are acceptable. Go to the **Microscope** settings in the toolbar, select **Engage Settings**, and ensure the default **Engage Parameters** are acceptable, modifying them if desired. (See SOP in **Supplementary Materials** for more details). Click the **Engage** button in the workflow to engage on the surface. Monitor the engage process to ensure that the tip engages properly.
NOTE: Upon clicking **Engage**, the **Tip Secured** notification at the bottom of the software screen will change to **Motor: ZZ.Z µm** where ZZ.Z is the distance the stepper motor has moved toward the sample surface. The probe should engage the surface at approximately the SPM Safety setting chosen in the Engage Settings (default value is 100 µm). If using a probe with a particularly long tip (i.e., large tip height), it may be necessary to increase the SPM Safety to avoid crashing the probe during the initial fast descent portion of the engage process (i.e., the SPM Safety must be greater than the probe tip height, defined as the distance from the cantilever to the end of the tip, plus the uncertainty in the surface focus distance).

7. Once engaged, switch the display type of the force curve from **Force vs Time** to **Force vs Z** by right-clicking on the curve and selecting **Switch Display Type**. Optimize the AFM topography and KPFM parameters in the **Parameters** window of the Scan interface (see the discussion and KPFM SOP in the **Supplementary Materials**). After defining an appropriate **Directory** path and **Filename** under **Capture > Capture Filename**, click the **Capture** icon to set up the capture of the desired next complete image, then click **Withdraw** in the workflow once the image has been captured (or alternatively click **Capture > Capture Withdraw** to automate the process).

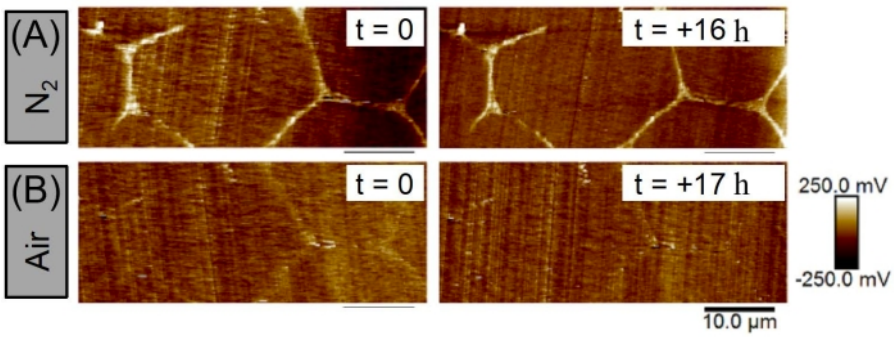

Figure 3: Effect of inert versus ambient atmosphere on KPFM Volta potential measurements. KPFM images of the same area of a binary MgLa alloy obtained in (**A**) dry N_2 and (**B**) ambient air on the same make and model of AFM with the same type of probe and imaging modality. In both cases, the sample was imaged twice with an overnight incubation between images. The images in air were obtained 1 day after the images in N_2. The results demonstrate that the KPFM contrast degraded with time upon exposure to ambient air as a thin passivating oxide layer formed on the alloy surface. Using the inert atmosphere (dry N_2) glovebox AFM system also allowed the use of lower lift heights, which can yield higher lateral spatial resolution. Scale bars = 10 µm. Abbreviations: KPFM = Kelvin probe force microscopy; AFM = atomic force microscopy. Please click here to view a larger version of this figure.

3. SEM, EDS, and EBSD imaging

NOTE: It is best to perform any electron microscopy or spectroscopy characterization **after** KPFM because the electron beam can deposit an unwanted carbon coating on the sample (i.e., electron beam deposition); this contamination layer will impact the VPD measured via KPFM (e.g., see **Figure 2** in Hurley et al.[18] or **Figure 1** in Mallinson and Watts[28]). Thin layers of carbon contamination can deposit even in very high vacuum conditions and will impact surface potential measurements.

1. Ensure that the sample inhibits charging. If the sample is insufficiently conductive (not typically the case for metal alloys), consider carbon coating prior to imaging. Load the sample into the SEM chamber. Close and vent the chamber; turn the laser on using the **Beam On** button. Zoom out optically using the magnification knob to obtain the maximum field of view (FOV) of the sample surface.
2. Locate the designated origin (e.g., nanoindentation, scratch, indelible ink dot, optical feature), then zoom in using the **Magnification** knob. Orient the X and Y axes according to the fiducial markers (i.e., adjust the sample orientation/rotation) by inputting values into the stage rotation and tilt options. Zoom in as needed and capture the desired images (e.g., secondary electron [SE], BSE, and EDS maps) of the designated ROI and save the files.
   NOTE: As SEM offers a wider FOV than AFM, it is often beneficial to obtain a large area SEM image to guarantee capturing the entire area to be co-localized with KPFM (see the discussion).

4. KPFM, SEM, EDS, and EBSD image overlay and analysis

1. Use appropriate software for each characterization tool (see **Table of Materials**) to process the raw data as needed. Save and export the acquired KPFM and SEM images in the desired file format(s) (e.g., *.spm, *.txt, *.jpg, *.tif, etc.) for the image overlay software to be used.
    1. Process KPFM data appropriately to ensure high-quality images (see the **Table of Materials**).
        NOTE: Depending upon the specific AFM hardware and software configuration employed, it is possible the sense (i.e., sign and relative ordering) of the measured VPDs may be reversed and need to be inverted. It is customary to report the VPD as the Volta potential of the sample minus that of the probe tip, with more noble/less easily oxidized surfaces indicated by a larger, more positive Volta potential, just as their work function would typically be reported as a large, positive value, indicating the relative difficulty of removing an electron from the surface.
        1. After opening the KPFM data file, apply a first order **Plane Fit** to the AFM topography (**Height Sensor**) channel of the KPFM images to remove the sample tip and tilt, as well as a first order **Flatten** if needed to compensate for any line-to-line offsets due to probe wear or picking up debris on the probe tip.
            NOTE: If absolute Volta potential measurements are desired (see the discussion) or multiple images containing KPFM VPDs measured with the same probe are to be compared, do not process the KPFM Volta potential channel (i.e., use the raw, as acquired data). If instead users are merely interested in the relative VPDs of microstructures internal to (i.e., contained wholly within) the sample region imaged, it is permissible to **Plane Fit** and **Flatten** the KPFM **Potential** channel as well to improve the image quality.
        2. Select the desired color scheme/gradient for the KPFM images by first selecting the **Potential** channel thumbnail on the left of the AFM topography image, then double-clicking on the **color scale bar** on the right of the KPFM VPD map to open the **Image Color Scale Adjust** window to the **Choose Color Table** tab.
        3. Enter an appropriate scale bar range (i.e., **Minimum** and **Maximum** value) for the KPFM VPD image in the **Modify Data Scale** tab of the **Image Color Scale Adjust** window, then click (i.e., **Minimum** and **Maximum** value). Repeat this process for the AFM topography image after first (re)-selecting the **Height Sensor** channel thumbnail image. Save **Journal Quality Exports** of the processed AFM topography image and KPFM VPD map as image files (e.g., *.jpg, *.tif, etc.).
2. Open the processed AFM topography image and KPFM VPD map, along with the raw SEM image, in the image manipulation software of choice (see **Table of Materials**). Identify the specified origin in both the AFM/KPFM data and SEM image(s) (e.g., SE, BSE, EDS, EBSD, etc.). Overlay the origins in the two images, then rotationally align the images using the X and Y coordinate axes designated by the chosen fiducial marks or characteristic features. Scale the images as needed.

NOTE: The topography features in AFM and SEM images should align with one another and may correspond with KPFM and compositional information (e.g., BSE image or EDS maps) due to differential polishing rates and VPDs for differing compositions. When overlaying and aligning images, it is often helpful to increase the transparency of the top (overlaid) image.

Representative Results

Binary Mg alloy: KPFM and SEM

Owing to their superior strength-to-weight ratios, magnesium (Mg) alloys are of interest for use in portable electronics and as structural components in transportation applications such as bicycles, cars, and airplanes. Additionally, Mg alloys are utilized for cathodic protection and as anodes in battery systems[33,34,35]. Pure Mg is not capable of forming a passive, protective oxide film due to it being too thin (the Pilling-Bedworth ratio of MgO is 0.81), which results in it being a highly active metal when alloyed with most other conductive materials (reduction potential of −2.372 V vs. the standard hydrogen electrode) [9]. A primary driving force of magnesium alloy corrosion is cathodic activation, where the cathodic reaction is enhanced by anodic dissolution[29]. One way to hinder this process is through microalloying with additions of metals that slow the cathodic hydrogen evolution reaction. A 2016 study examined the incorporation of germanium (Ge) as a microalloying element to produce a binary Mg alloy[29]. KPFM indicated the presence of regions of differing Volta potentials and quantified the corresponding VPDs; however, this result alone could not distinguish the elemental make-up of these regions. By co-localizing KPFM with BSE SEM (which provides elemental contrast based on atomic number), as shown by the overlaid images in **Figure 4**, the relative nobilities (i.e., sites of likely anodic/cathodic behavior) of the matrix and Mg_2Ge secondary phase were accurately identified. During active corrosion, the Mg_2Ge secondary phase was observed as a preferential site for reduction, which, in turn, shifted the corrosion mechanism from widespread, filiform-like corrosion on Mg to reduced attack at minimal sites when Ge was included, thereby improving the corrosion performance of the material.

Cu-Ag-Ti ternary braze alloy: KPFM and SEM/EDS

Brazing is a lower-temperature alternative to other common metal-joining techniques such as welding[36]. However, joint performance and lifetime can suffer due to phase separation and resultant galvanic corrosion within the braze[37], as shown in a comparative study on the use of Cu-Ag-Ti (CuSil) and Cu-Ag-In-Ti (InCuSil) brazes to join 316L stainless steel coupons[30]. **Figure 5** shows a representative region of a Cu-Ag-Ti braze joint, where co-localized BSE SEM, EDS, and KPFM confirmed that the silver-rich phase was cathodic to (i.e., more noble than) the copper-rich phase by ~60 mV, with this phase separation and VPD eventually leading to the initiation of microgalvanic corrosion within the copper-rich regions of the braze. However, the surrounding 316L stainless steel coupons and titanium (Ti) interfacial wetting layer[38] were observed to be anodic in Volta potential to both the neighboring braze alloy phases. Thus, the stainless steel matrix would, in theory, be more reactive (i.e., more easily oxidized) than the braze. However, in a galvanic corrosion scenario, the worst case is to have a small anode in contact with a large cathode, as the greater cathodic surface area will drive rapid anodic dissolution. Conversely, in this scenario involving anodic 316L stainless steel coupons joined by a cathodic braze alloy, the combination of a larger anode and a smaller cathode should serve to slow the rate of galvanic corrosion.

Two-phase ternary Ti alloy + boron: KPFM and SEM/EDS

Wrought titanium alloy with 6 at. % aluminum and 4 at. % vanadium (Ti-6Al-4V, or Ti64) is an attractive structural alloy due to its high strength-to-weight ratio and excellent corrosion resistance[39,40,41]. In particular, Ti64 finds use in biomedical implants and devices due to its biocompatibility[42,43,44]. However, because Ti64 is stiffer than bone, it can lead to bone deterioration and poor implant adherence when employed for joint replacements. Additions of boron (B), which has a solubility limit of ~0.02 at. % in Ti64, have been investigated to tune the mechanical properties of Ti64 to more closely mimic those of bone[31]. However, such boron additions could result in increased susceptibility of the alloy to corrosion, particularly when subjected to extended contact with blood plasma as in the case of biomedical implants such as joint replacements. **Figure 6** shows co-localized KPFM, BSE SEM, and EDS maps of a Ti64 + 0.43% B sample. The resultant boron-rich TiB needles (**Figure 6A** and **Figure 6D**) that appear above the saturation point for boron could be distinguished from the surrounding Al-rich Ti64 alpha (α) matrix (**Figure 6C**) and interconnected filamentous V-rich Ti64 beta (β) phase, with the TiB needles appearing at a slightly higher (i.e., more noble) Volta potential (brighter in **Figure 6B**) than the β phase[31]. **Figure 7** illustrates the fact that KPFM is significantly more surface-sensitive than SEM due to differences in the penetration depth and sampling volume of the two techniques. Specifically, the formation of a few nanometers thick passivating oxide on the alloy surface upon exposure to a solution mimicking human plasma and the subsequent potentiodynamic cycling (ASTM F2129-15 standard test protocol to determine the corrosion susceptibility of implant devices) resulted in measuring a relatively uniform surface potential (**Figure 7B**) despite the sub-surface microstructure remaining visible in the BSE SEM image (**Figure 7A**) and EDS maps (**Figure 7C**). In contrast, upon subjecting Ti64 samples to forced corrosion conditions (i.e., high salt concentration and extreme anodic potential), it was possible to employ co-localized KPFM, BSE SEM, and EDS to observe differences in corrosion behavior for low (0.04% B) versus high (1.09% B) concentration boron added samples (**Figure 8**).

3D printed ternary Ti alloy: KPFM and SEM/EBSD

Additive manufacturing (AM) of metals and metal alloys has the potential to produce parts cheaper and faster, with more complex shapes and control over microstructure and properties[45]. One of the leading materials used in AM is Ti64, as described above. Similar to wrought Ti64, AM Ti64 contains two phases, the thermodynamically stable Al-rich α phase and the metastable V-rich β phase, with each phase exhibiting a range of crystallographic orientations. Depending on which phase and crystallographic orientations are present at the surface, the corrosion properties of the printed part will be affected. **Figure 2** presents co-localized AFM/KPFM, SEM (both SE and BSE), and EBSD (both α and β phase) images of AM Ti64 produced via electron beam melting powder bed fusion followed by hot isostatic pressing (HIP)[32]. The crystallographic orientation of different grains as revealed by EBSD was co-localized with KPFM VPDs to determine which orientation(s) are likely to affect the corrosion properties of AM Ti64 so that build process parameters can be tuned to reduce non-ideal orientations or phases. The topography (**Figure 2E**) and VPD (**Figure 2F**) acquired by KPFM overlay the slightly rotated large square area demarcated by the dotted white lines in the SEM (**Figure 2A,B**) and EBSD (**Figure 2C,D**) maps. **Figure 9** zooms in on the area outlined by the solid white rectangles in **Figure 2A-D**, showing that the measured VPD upon going across an α-α grain boundary depends upon the relative crystallographic orientations of the two grains. Additionally,

α-β phase boundaries exhibited a relative VPD equal to or greater than α-α boundaries of dissimilar grain orientation. This is important, as a higher Volta potential gradient will theoretically result in greater intergranular corrosion rates due to the increased microgalvanic driving force, suggesting a need to minimize the number of β grains and their contact points with α laths.

Cross-sectional analysis of Zr alloys for nuclear cladding: KPFM, SEM, and Raman

Zirconium (Zr) and its alloys are commonly used as cladding in nuclear applications because of their low neutron absorption cross-section and high-temperature corrosion resistance. However, due to a variety of potential degradation mechanisms, including the "breakaway phenomenon", hydride-induced embrittlement, and various pellet-cladding interactions, zirconium lifetime can be drastically shortened, resulting in the risk of nuclear reactor failure[46]. Thus, zirconium alloy degradation mechanisms were investigated by co-localization of KPFM, SEM, and confocal scanning Raman microscopy (which can reveal differences in crystal structure based on the Raman spectrum) [47]. Here, a correlation between zirconium oxide crystal structure (monoclinic versus tetragonal) and relative Volta potential was observed. Specifically, the tetragonal-rich zirconium oxide (t-ZrO_2) preferentially located near the metal-oxide interface (indicated by the vertical dashed line in the right-hand panels of **Figure 10A-C** and **Figure 10E-G**) was found to be significantly more active (i.e., more likely to oxidize/corrode) compared to the ~600 mV more noble bulk monoclinic-rich zirconium oxide (m-ZrO_2). This is seen in the VPD and percent tetragonality line cross-sections across the ZrO_2/Zr interface in **Figure 10A-C**. Further, the t-ZrO_2 region was discovered to also be slightly active relative to the metal substrate (**Figure 10A**), resulting in a p-n junction region as another step in the otherwise diffusion-limited oxidation of zirconium.

Further evidence of the utility of KPFM and co-localization with complementary characterization techniques is also seen in this work. Even in nominally "pure" Zr metal, some trace iron impurities remain present after processing, resulting in iron-rich secondary phase particles (Fe-rich SPPs). This was observed via KPFM and scanning confocal Raman spectral mapping, where the large increase in relative Volta potential corresponding to the bright cathodic particle visible in **Figure 10E** correlated with a significant change in the Raman spectrum (**Figure 10F,G**). This cathodic particle was initially presumed to be an Fe-rich SPP, but EDS was unable to provide confirmation of the presence of iron in this case (**Figure 10H**). However, for the data presented in **Figure 10**, KPFM was performed first, followed by Raman mapping, and then finally SEM/EDS. Unfortunately, laser beam damage (including ablation/removal of SPPs) is possible during Raman mapping depending upon the incident laser power, potentially making the identification of SPPs via subsequent EDS impossible. The deleterious effect of the incident Raman excitation laser was confirmed here by removing Raman mapping from the sequential characterization process, leading to successful identification of Fe-rich SPPs and their corresponding increased VPD relative to the surrounding Zr matrix by co-localized KPFM and SEM/EDS (red circles in **Figure 11A,B**). This underscores the importance of the order in which a user employs co-localized characterization techniques, as some tools are more likely to be destructive or affect the surface. Specifically, while KPFM is non-destructive, performing Raman or SEM/EDS analysis prior to KPFM can impact the resulting Volta potential measurements[18,28]. It is, therefore, highly recommended that KPFM be performed first when co-

localizing with more potentially damaging surface-sensitive techniques.

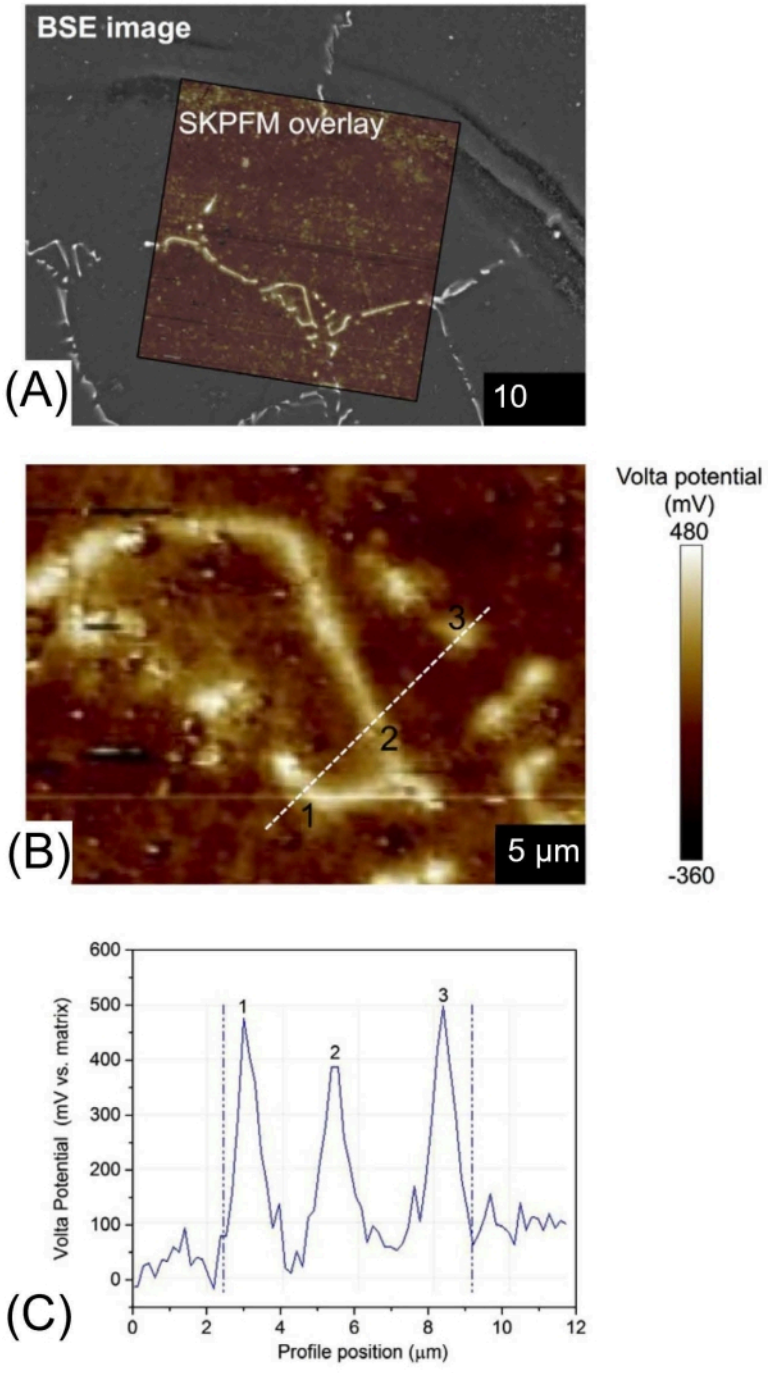

Figure 4: Co-localization of KPFM and BSE SEM. (**A**) Overlaid BSE SEM and KPFM images of a binary Mg-0.3Ge alloy, (**B**) zoom of overlaid KPFM Volta potential map in **A** showing the relative potentials of the Mg_2Ge secondary phase (brighter,

more noble) and matrix (darker), and (**C**) line scan data for the Volta potential corresponding to the dashed line region in **B** showing the ~400 mV difference in potential between the matrix and Mg_2Ge secondary phase. This figure is reproduced from Liu et al.[29]. Scale bars = (**A**) 10 µm, (**B**) 5 µm. Abbreviations: KPFM = Kelvin probe force microscopy; SEM = scanning electron microscopy; BSE = back scattered electron. Please click here to view a larger version of this figure.

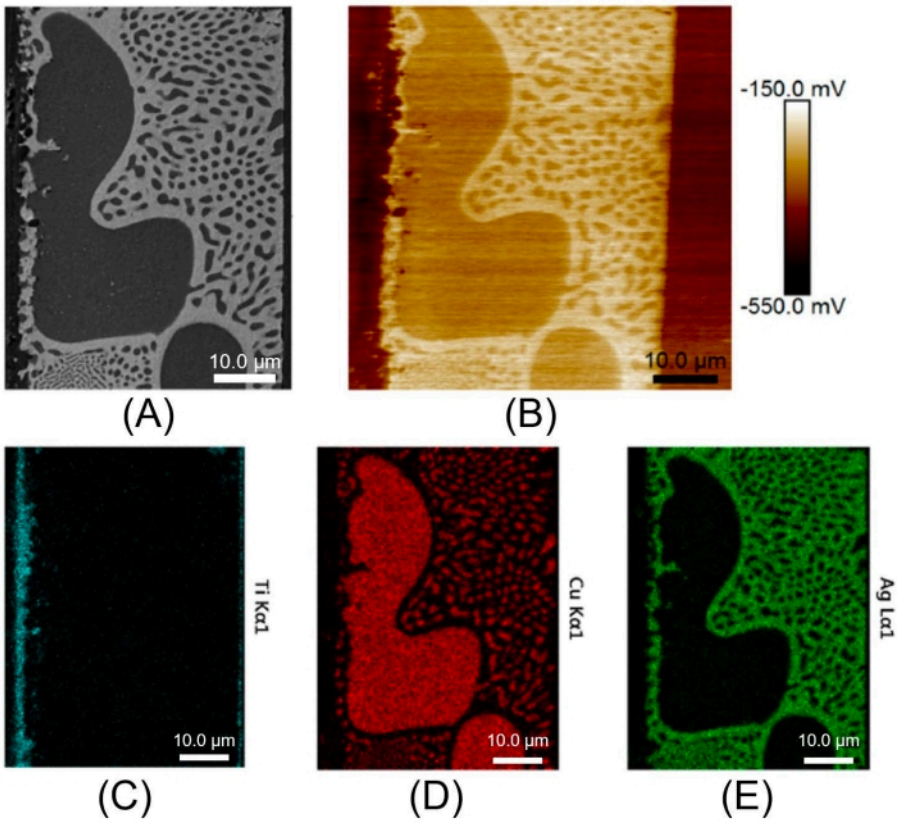

Figure 5: Co-localization of KPFM, BSE SEM, and EDS. (**A**) BSE SEM image of a Cu-Ag-Ti (CuSil) braze sample and (**B**) corresponding co-localized KPFM surface potential image. EDS elemental maps of the identical region of the ternary alloy for (**C**) titanium (Ti) wetting additive, (**D**) copper (Cu), and (**E**) silver (Ag) are also shown. Scale bars = 10 µm. This figure is reproduced from Kvryan et al.[30]. Abbreviations: KPFM = Kelvin probe force microscopy; SEM = scanning electron microscopy; BSE = back scattered electron; EDS = energy dispersive spectroscopy. Please click here to view a larger version of this figure.

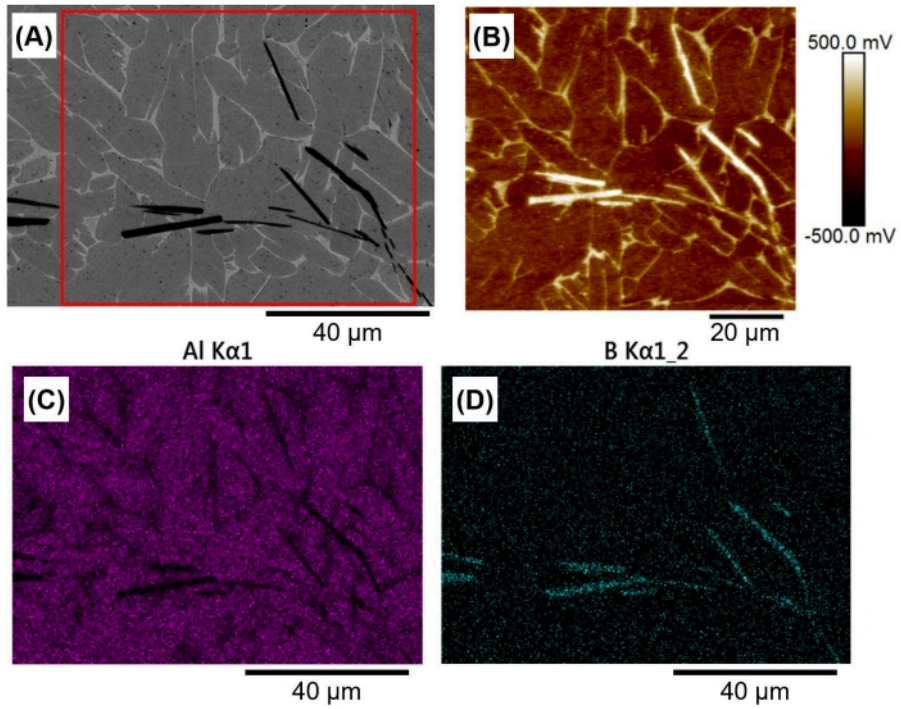

Figure 6: Co-localization of KPFM, BSE SEM, and EDS in a modified alloy. Co-localized (**A**) BSE SEM and (**B**) KPFM images of Ti-6Al-4V alloyed with 0.43% B showing the formation of boron-rich needles, with corresponding EDS maps of (**C**) aluminum (Al) and (**D**) boron (B). Red box in the SEM image indicates the location of the KPFM scan. Scale bars = (**A,C,D**) 40 µm, (**B**) 20 µm. This figure is adapted from Davis et al.[31]. Abbreviations: KPFM = Kelvin probe force microscopy; SEM = scanning electron microscopy; BSE = back scattered electron; EDS = energy dispersive spectroscopy. Please click here to view a larger version of this figure.

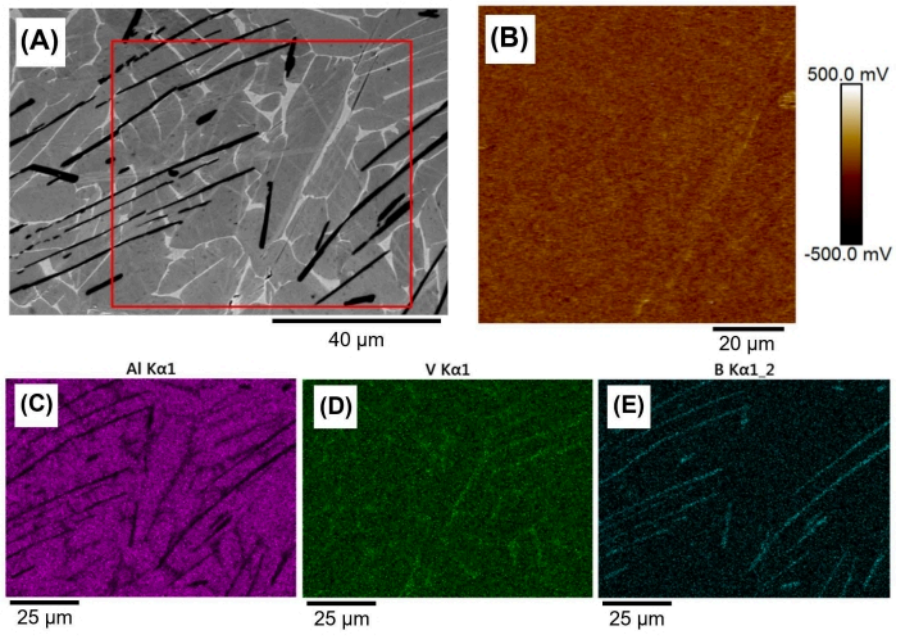

Figure 7: Surface passivation and differential imaging depth of KPFM versus BSE SEM and EDS. Co-localized (**A**) BSE SEM and (**B**) KPFM images of a Ti-6Al-4V + 1.09% B sample subjected to the ASTM F2129-15 test protocol. The formation of a thin passivating layer resulted in a more uniform surface potential as measured by KPFM compared with samples not subjected to the ASTM F2129-15 test protocol (see **Figure 6**). Co-located (**A**) BSE SEM and (**C**) EDS maps (aluminum, Al; vanadium, V; boron, B) confirmed the phase composition of the microstructure beneath the passive film and the lack of evident corrosion attack. Red box in the SEM image indicates the approximate location of the corresponding KPFM scan. Scale bars = (**A**) 40 µm, (**C–E**) 25 mm, (**B**) 20 µm. This figure is reproduced from Davis et al.[31]. Abbreviations: KPFM = Kelvin probe force microscopy; SEM = scanning electron microscopy; BSE = back scattered electron; EDS = energy dispersive spectroscopy. Please click here to view a larger version of this figure.

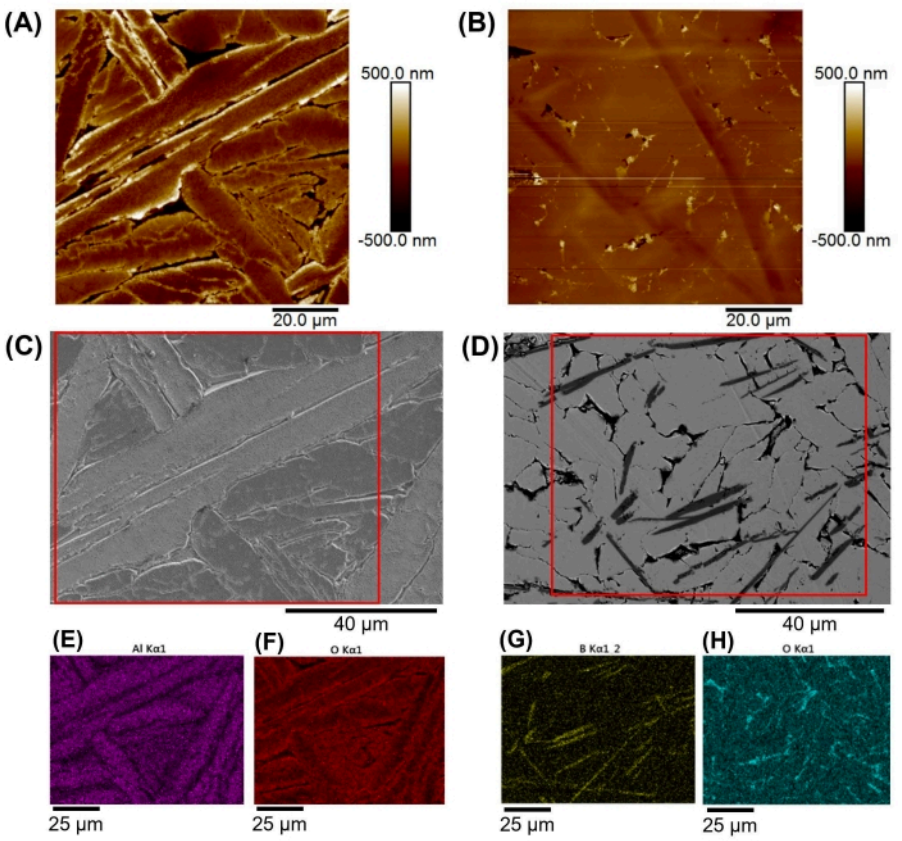

Figure 8: Evidence of preferential corrosion. (**A,B**) AFM topography and (**C,D**) BSE SEM images of (**A,C,E**) 0.04% B and (**B,D,F**) 1.09% B Ti-6Al-4V samples with corresponding (**E**) aluminum (Al) and oxygen (O) and (**F**) boron (B) and oxygen (O) EDS maps. Red boxes on the (**C,D**) SEM images indicate the approximate location of (**A,B**) the corresponding AFM images. (**A,B**) Pitting visible in the AFM topography images shows that corrosion preferentially occurred within the vanadium-rich metastable β phase despite its higher Volta potential. (**B,D,F**) Note also that the higher boron content sample exhibited significantly less (and shallower) pitting. Scale bars = (**A,B**) 20 µm, (**E–H**) 25 mm, (**C,D**) 40 µm. This figure is reproduced from Davis et al.[31]. Abbreviations: AFM = atomic force microscopy; SEM = scanning electron microscopy; BSE = back scattered electron; EDS = energy dispersive spectroscopy. Please click here to view a larger version of this figure.

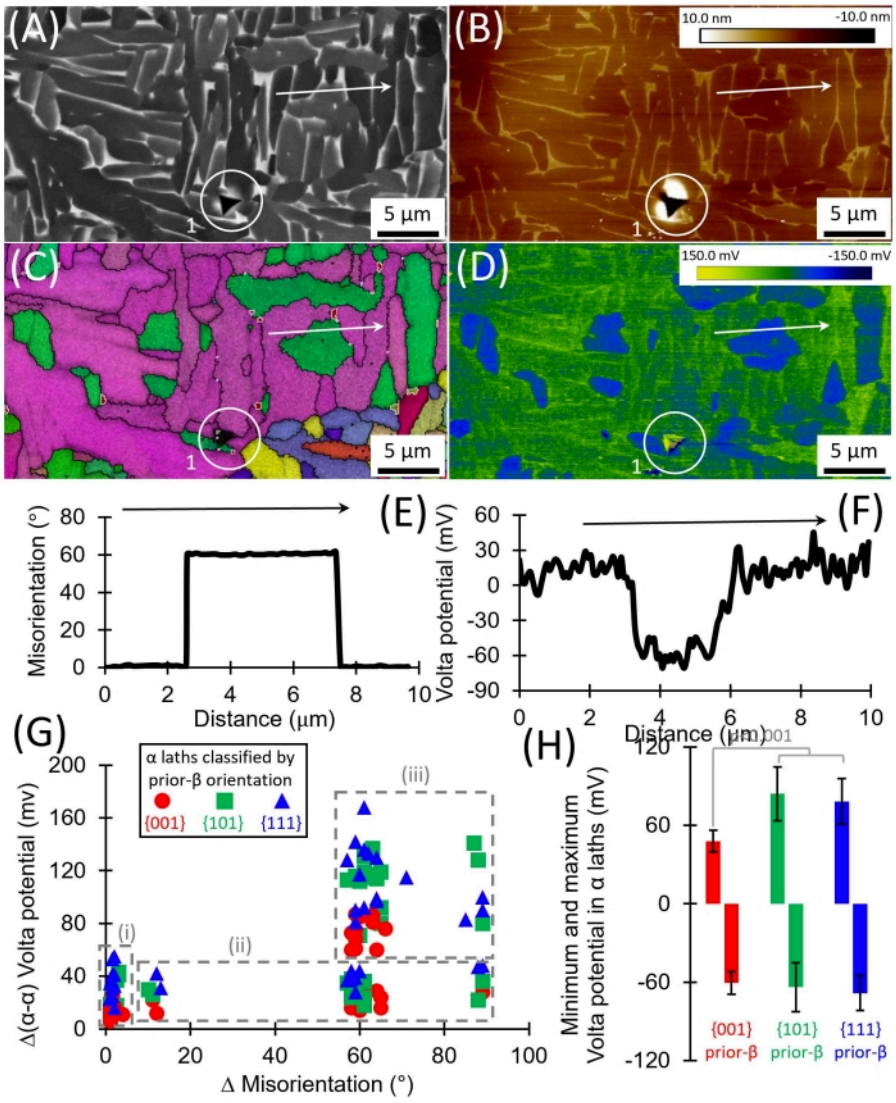

Figure 9: Co-localization of KPFM, BSE SEM, and EBSD. Detailed SEM and KPFM analysis of the area designated by the solid rectangle in **Figure 2**. Technique for characterizing α laths by co-locating: (**A**) BSE imaging, (**B**) AFM height sensor (topography), (**C**) EBSD (white lines indicate α-β phase boundaries, black lines designate defined grain boundaries), and (**D**) KPFM Volta potential. The results from line scans across hypermaps indicated by the white arrows in **A–D** are shown for (**E**) EBSD and (**F**) KPFM Volta potential. (**G**) Summaries of relative differences in Volta potential are shown for three types of measurements: i) within a single α lath, ii) across α-α boundaries of similar grain orientation and iii) across α-α boundaries of differing grain orientation. (**H**) Ranges of Volta potential for different prior-*β* orientations (one standard deviation shown). Scale bars = (**A–D**) 5 µm. This figure is reproduced from Benzing et al.[32]. Abbreviations: KPFM = Kelvin probe force

microscopy; SEM = scanning electron microscopy; BSE = back scattered electron; AFM = atomic force microscopy; EBSD = electron backscattered diffraction. Please click here to view a larger version of this figure.

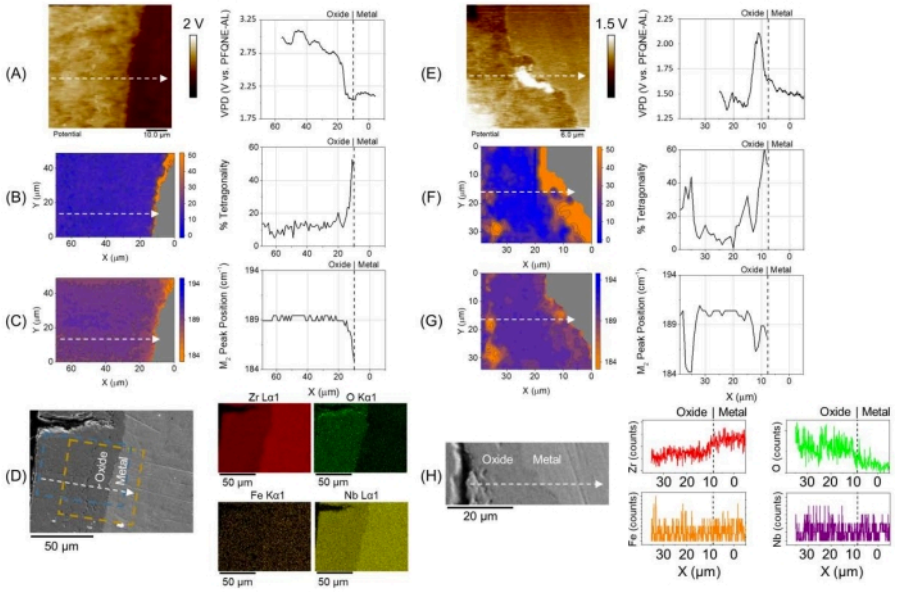

Figure 10: Co-localization of KPFM, Raman microscopy, BSE SEM, and EDS. Co-localization of KPFM, Raman microscopy, and SEM/EDS for oxidized and cross-sectioned (**A–D**) Zr-2.65Nb alloy and (**E–H**) pure Zr. From top to bottom: (**A,E**) KPFM Volta potential maps (left) with corresponding representative VPD line scans (right), (**B,F**) percent tetragonality and (**C,G**) monoclinic ZrO2 peak position maps (indicative of compressive stress) determined via Raman mapping with corresponding representative line scans, and (**D,H**) SEM images with corresponding EDS maps and representative line scans. In all cases, the locations of line scans are indicated by white arrows in the corresponding sample images. Scale bars = (**A**) 10 µm, (**D**) 50 µm, (**E**) 6 µm, (**H**) 20 µm. This figure is adapted from Efaw et al.[47]. Abbreviations: KPFM = Kelvin probe force microscopy; SEM = scanning electron microscopy; BSE = back scattered electron; EDS = energy dispersive spectroscopy. Please click here to view a larger version of this figure.

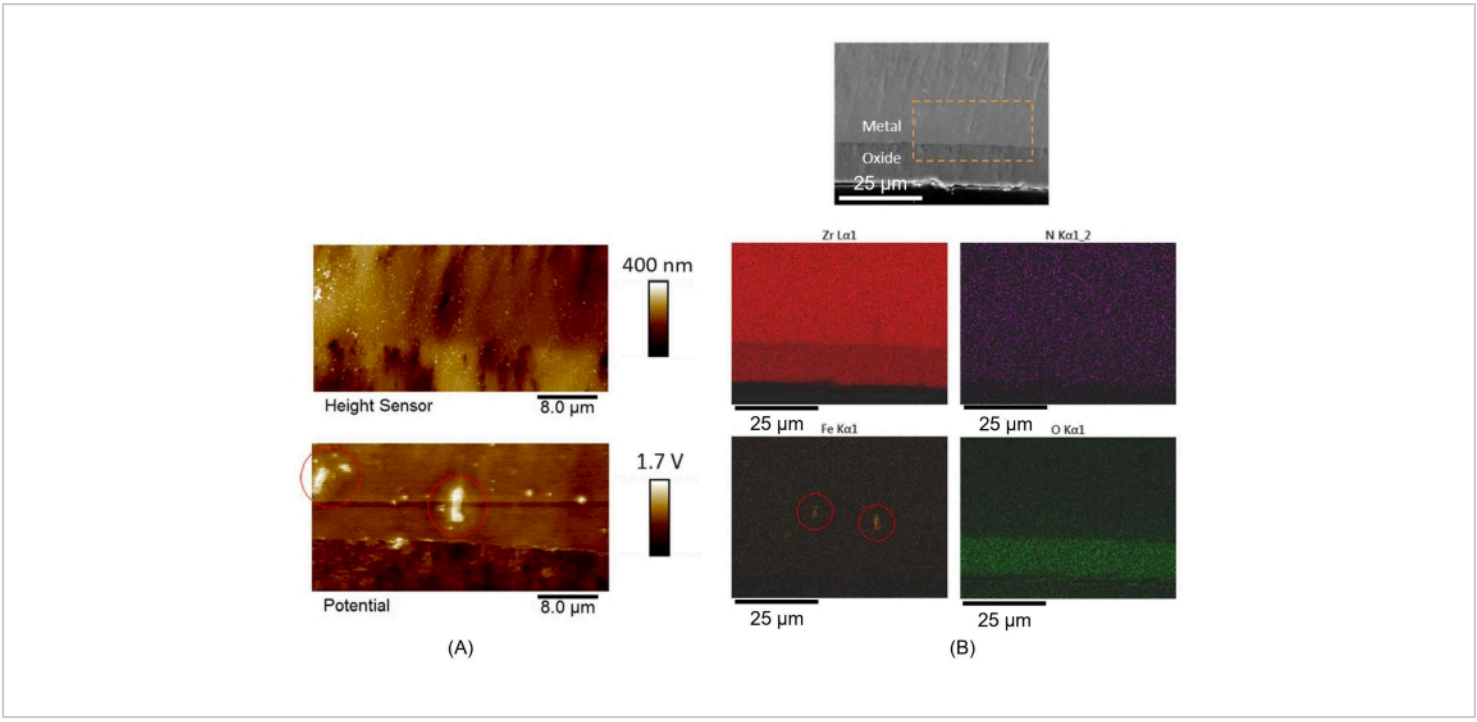

Figure 11: Co-localization of KPFM, BSE SEM, and EDS without Raman microscopy. Co-localization of (**A**) KPFM height (top) and Volta potential (bottom) maps with (**B**) SEM (top) and EDS elemental analysis (bottom) on a cross-sectioned sample of oxidized pure Zr (pre-breakaway). The area where KPFM was performed is indicated by the dashed line orange rectangle in the SEM image on the top right, while the red circles in the KPFM Volta potential and EDS Fe abundance maps indicate the correlation between high VPD regions and Fe-rich particles. Scale bars = (**A**) 8 µm, (**B**) 25 µm. This figure is reproduced from Efaw et al.[47]. Abbreviations: KPFM = Kelvin probe force microscopy; SEM = scanning electron microscopy; BSE = back scattered electron; EDS = energy dispersive spectroscopy. Please click here to view a larger version of this figure.

Supplementary Material: Standard operating procedure for Kelvin probe force microscopy. Please click here to download this File.

Discussion

As KPFM measures surface topography and VPDs with nanoscale resolution, sample preparation is crucial for obtaining high-quality KPFM images. The finely gradated polishing steps discussed in the protocol section are an optimal starting point for achieving a high-quality final surface finish for metal alloys. In addition, examining the surface after each polishing step with an optical microscope can confirm improving surface quality (e.g., reduced number, size, and depth of visible scratches), while finishing with a vibratory polisher will offer the best final surface quality. Finally, one must consider solvent compatibility with the sample and mounting agent when choosing polishing compounds and cleaning methods. In addition to careful sample preparation, co-localizing different characterization techniques requires the use of a common reference (i.e., fiducial mark) to indicate the origin location and XY coordinate axes directions (i.e.,

sample orientation/rotation) [6,7,32]. There are a variety of possible methods to accomplish this. The simplest method is to identify distinct, preexisting features on the surface that can be seen by eye or with the aid of an optical microscope. For this method to work, the feature needs to have a well-defined, easily identifiable origin point (e.g., a corner or protrusion) and exhibit a clear orientation. The CuSil braze sample described here demonstrated micron-scale features meeting these requirements, making co-localization straightforward (**Figure 1** and **Figure 5**) [30]. Furthermore, the distinctive visible colors of the two phase-separated regions provided insight into their composition (i.e., copper vs. silver-rich). Perhaps the best, most reproducible method for creating fiducial marks is nanoindentation, although this requires access to a standalone nanoindenter or AFM-integrated nanoindenter system. Nanoindents can be arranged in a variety of ways, but the most obvious is to use one indent as an origin and two additional indents aligned along orthogonal axes to indicate the X and Y directions from the origin, as shown in the AM Ti64 example (**Figure 2**) [32]. Finally, fiducial marks can also be established by scratching or marking the surface (e.g., with a diamond scribe, razor blade, or micromanipulator probe tip; or indelible ink or permanent marker). Scratch fiducials can be beneficial when distinct surface features and/or a nanoindenter are not available; however, these methods can cause issues, particularly when examining corrosion properties (e.g., a scratch can damage the surface, causing it to be susceptible to corrosion). If using a scratch fiducial, one should place the scratch a bit farther from the examined surface to help ensure the scratch does not affect the experimental results. Likewise, contamination from ink may impact corrosion performance, and hence, these methods are better used when studying material properties other than corrosion.

As quantification of the VPD in KPFM depends upon the application of both an AC bias and a DC nulling potential, the path from the sample surface to the AFM chuck must be electrically continuous. Thus, if the sample is somehow electrically insulated from the chuck (e.g., it has a backside oxide coating, is deposited on a non-conducting substrate, or is covered by epoxy), then a connection will need to be made. One solution is to use silver paste (see the **Table of Materials**) to draw a line from the top surface of the sample to the chuck, ensuring the line has no breaks and is completely dry prior to imaging. Copper tape or conductive carbon tape can also be used to create a similar electrical connection. Regardless of the method used to establish the electrical connection, the chuck-sample continuity should be checked with a multimeter prior to KPFM imaging.

Oxidation or contamination of a metal surface leads to drastic changes in measured VPDs. Minimizing the amount of oxygen the sample comes into contact with can slow down surface passivation or degradation. One way to prevent oxidation is by placing the AFM in an inert atmosphere glovebox. By replacing the oxygen-rich ambient environment with an inert gas such as argon or nitrogen, the sample surface can be maintained in a relatively pristine condition for an extended period (**Figure 3**). An additional benefit of employing a glovebox is the elimination of surface water, which can introduce dissolved contaminants, accelerate corrosion or passivation, and degrade the resolution due to the need for increased lift heights (see below). Additionally, the measured VPD has been shown to be sensitive to the relative humidity[15,23], and it is, therefore, important to monitor (and ideally report) the relative humidity if KPFM experiments are performed under ambient conditions.

Depending on the AFM used (see the **Table of Materials**) and the KPFM implementation mode employed, the available imaging parameters and nomenclature will vary. However, some general guidelines can be formulated. KPFM combines AFM topography with VPD measurements. Thus, a good topography image is an essential first step, with a setpoint chosen to minimize the tip-sample force (and hence, the potential for tip wear and sample damage) while still maintaining high-fidelity tracking of the topography (through optimizing the interplay of the gains and setpoint). In other words, regardless of the topography imaging mode, the user must determine a balance between sufficient interaction with the surface without damaging the sample or probe (particularly if it is metal-coated). Additionally, if the sample is dirty or not polished well, the probe tip may come into contact with debris, resulting in a broken tip or tip artifacts. It is also imperative to avoid topographical artifacts in the KPFM Volta potential channel, which is more easily achieved in a dual pass KPFM mode such as the one described here. Optimal KPFM imaging requires a balance between lower and higher lift heights, as the lateral resolution of KPFM decreases with increasing lift height, but short-range van der Waals forces (which are responsible for the tip-sample interactions that underpin AFM topography measurements) can produce instabilities that affect the measurement of the longer-range electrostatic interaction at lower lift heights. Working in an inert atmosphere glovebox as described above can be beneficial in this regard, as elimination of the layer of surface water removes its contribution to the tip-sample interaction for improved feedback, thereby enabling lower KPFM lift heights and improved spatial resolution, with the additional benefit of more reproducible VPDs due to constant (essentially zero) humidity and reduced charge screening. Likewise, decreased surface roughness (i.e., better polishing) can enable lower lift heights and result in improved KPFM resolution, as a good rule of thumb to avoid topographical artifacts is to set the lift height approximately equal to the height of the tallest high aspect ratio surface feature(s) present within the scan region. Another factor that comes into play in determining the optimal lift height is the probe oscillation amplitude during the lift mode pass-larger amplitude confers greater sensitivity to small VPDs, but at a cost of necessitating larger lift heights to avoid topographical artifacts or striking the surface (often visible as abrupt spikes in the lift scan phase). Again, the smoother the surface, the lower the lift height that can be achieved for a given oscillation amplitude, thereby improving both spatial resolution and Volta potential sensitivity-good sample preparation is key. Finally, when capturing a KPFM image, one should keep in mind that a larger scan size allows for more sample coverage but at the cost of increased scan time, as slow scan rates are required to allow the accurate measurement of Volta potentials by the detection electronics.

Inference about the relative nobility of microstructures observed on the surface of a conductive material can be made from VPDs measured using KPFM (e.g., microgalvanic couples, intergranular corrosion, pitting corrosion). However, the absolute Volta potentials of materials reported in the literature vary widely[18,24,27]. This lack of reproducibility has resulted in misinterpretations about different materials systems and their corrosion behavior[23,25]. As a result, for the determination of absolute Volta potentials (i.e., work functions) or comparison of VPDs measured across labs, probes, or days, calibration of the KPFM probe's work function relative to an inert material (e.g., gold) is essential[25,48]. A 2019 study by some of the authors examined different KPFM probes and showed the variability of the resulting measured VPD between those probes and an aluminum-silicon-gold (Al-Si-Au) standard. Differences in work function were even observed for individual probes of the same nominal

material and design (**Figure 12**)[25]. As a proof of concept, the 316L stainless steel joined together by a CuSil braze previously referenced was used as an exemplary material for measuring absolute VPDs or work functions. The data from the 2016 work by Kvryan et al.[30] was compared with KPFM VPDs obtained on the same sample with a variety of probes and used to analyze the inner-braze Volta potentials. By calibrating the probe work function using the Au portion of the Al-Si-Au standard as a reference work function, the repeatability of the measured VPD of the braze phases improved by over an order of magnitude, from several hundred millivolts (**Figure 12A**) to tens of millivolts (**Figure 12C**). Further improvements in calibration can be realized by directly measuring the work function of the inert reference (e.g., via photoemission spectroscopy or Auger electron spectroscopy) or calculating the work function using density functional theory[25,48].

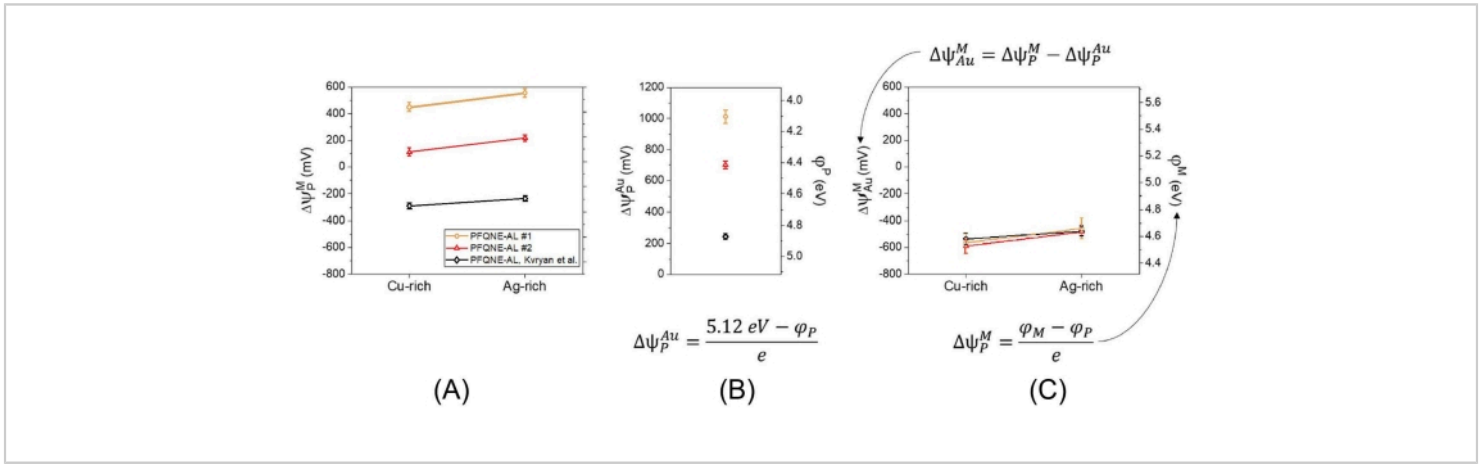

Figure 12: Effect of probe calibration on KPFM Volta potential reproducibility. (**A**) VPDs for copper-rich and silver-rich regions within the CuSil braze sample obtained relative to three different PFQNE-AL probes. (**B**) VPDs for the same three probes relative to the gold portion of the Al-Si-Au standard presented on the left ordinate axis, with resulting modified PFQNE-AL work function values presented on the right ordinate axis, as calculated from density functional theory. (**C**) Absolute VPDs of the copper-rich and silver-rich regions obtained by scaling the measured VPDs relative to the gold of the Al-Si-Au standard imaged prior to imaging of the braze sample. The left ordinate axis (calculated using the equation above panel **C**) indicates the VPD between the braze sample phases and the gold standard. The right ordinate axis (calculated using the equation below panel **C**) presents the resultant modified work function for each phase based on the modified work function of the probe calculated in panel **B**. This figure is reproduced from Efaw et al.[25]. Abbreviations: KPFM = Kelvin probe force microscopy; VPD = Volta potential difference. Please click here to view a larger version of this figure.

In conclusion, the co-localization of KPFM Volta potential maps with advanced SEM techniques, including SE images, BSE images, EDS elemental composition maps, and EBSD inverse pole figures can provide insight into structure-property-performance relationships. Likewise, other nano- to microscale characterization techniques such as scanning confocal Raman microscopy can be co-localized as well to provide further structural insight. However, when co-localizing

multiple characterization tools, sample preparation is crucial, including both minimizing surface roughness and debris, as well as identifying or creating reliable fiducial markers to indicate the sample imaging origin and axes (i.e., orientation or rotation). Additionally, the potential impact of a given characterization technique on subsequent measurements must be taken into consideration, and for this reason, it is preferable that KPFM (which is both nondestructive and highly sensitive to surface contamination) be performed first prior to other characterization methods. Finally, it is important to minimize surface contaminants, take into account and monitor (or better yet, eliminate) the confounding effects of the testing environment (e.g., ambient humidity), and properly calibrate the work function of the KPFM probe to enable the reliable, meaningful comparison of KPFM Volta potential measurements reported in the literature. To this end, the use of an inert atmosphere glovebox to house the AFM system (or, if not available, employing another form of humidity control/ low-moisture environment) and a gold or other inert reference material standard with a well-characterized work function for probe calibration are recommended.

Disclosures

The authors have no conflicts of interest to disclose.

Acknowledgments

Except as specifically noted below, all AFM and KPFM imaging was performed in the Boise State University Surface Science Laboratory (SSL), as was the co-localized scanning confocal Raman microscopy, with co-localized SEM/EDS imaging performed in the Boise State Center for Materials Characterization (BSCMC). The glovebox AFM system used in much of this work was purchased under National Science Foundation Major Research Instrumentation (NSF MRI) Grant Number 1727026, which also provided partial support for PHD and OOM, while the Raman microscope was purchased with funding from the Micron Technology Foundation. The authors thank Micron Technology for the use of their glovebox AFM system in securing preliminary data for the MRI grant, including acquiring the inert atmosphere KPFM images of the binary MgLa alloy shown in **Figure 3** of this manuscript. Partial support for OOM and MFH was also provided by NSF CAREER Grant Number 1945650, while CME and MFH acknowledge additional funding from the NASA Idaho Space Grant Consortium EPSCoR Seed Grant. FWD was supported by the Center for Integrated Nanotechnologies, a Department of Energy Office of Basic Energy Sciences user facility. Sandia National Laboratories is a multimission laboratory managed and operated by National Technology and Engineering Solutions of Sandia LLC, a wholly owned subsidiary of Honeywell International Inc., for the U.S. Department of Energy National Nuclear Security Administration under contract DE-NA0003525.

The authors thank Jasen B. Nielsen for preparation of the braze samples for KPFM imaging. The binary MgLa alloy (**Figure 3**) was provided by Nick Birbilis, formerly of Monash University, Australia, with support from the U.S. Army Research Laboratory (Agreement Number W911NF-14-2-0005). Kari (Livingston) Higginbotham is gratefully acknowledged for her KPFM imaging and analysis contributions to the Cu-Ag-Ti braze sample. Nik Hrabe and Jake Benzing of the National Institute of Standards and Technology (NIST) are acknowledged for helpful discussions, as well as their extensive contributions in preparing (including printing, polishing, and creating nanoindentation fiducials) and performing SEM/EBSD analysis at NIST on the AM

Ti-6Al-4V sample while Jake Benzing held a National Research Council Postdoctoral Research Associateship.

This paper describes objective technical results and analysis. Any subjective views or opinions that might be expressed in the paper are those of the author(s) and do not necessarily represent the views of the U.S. Department of Energy, National Aeronautics and Space Administration, National Institute of Standards and Technology, National Science Foundation, or the United States Government.

References

1. Borgani, R. et al. Intermodulation electrostatic force microscopy for imaging surface photo-voltage. *Applied Physics Letters.* **105** (14), 143113 (2014).
2. Femenia, M., Canalias, C., Pan, J., Leygraf, C. Scanning Kelvin probe force microscopy and magnetic force microscopy for characterization of duplex stainless steels. *Journal of the Electrochemical Society.* **150** (6), B274 (2003).
3. Sathirachinda, N., Pettersson, R., Pan, J. Depletion effects at phase boundaries in 2205 duplex stainless steel characterized with SKPFM and TEM/EDS. *Corrosion Science.* **51** (8), 1850-1860 (2009).
4. Kvryan, A. et al. Corrosion initiation and propagation on carburized martensitic stainless steel surfaces studied via advanced scanning probe microscopy. *Materials.* **12** (6), 940 (2019).
5. Kharitonov, D. S. et al. Surface and corrosion properties of AA6063-T5 aluminum alloy in molybdate-containing sodium chloride solutions. *Corrosion Science.* **171**, 108658 (2020).
6. Green, C. M., Hughes, W. L., Graugnard, E., Kuang, W. Correlative super-resolution and atomic force microscopy of DNA nanostructures and characterization of addressable site defects. *ACS Nano.* **15** (7), 11597-11606 (2021).
7. Klein, W. P. et al. Multiscaffold DNA origami nanoparticle waveguides. *Nano Letters.* **13** (8), 3850-3856 (2013).
8. Heusler, K. E., Landolt, D., Trasatti, S. Electrochemical corrosion nomenclature (Recommendations 1988). *Pure and Applied Chemistry.* **61** (1), 19-22 (1989).
9. Jones, D. *Principles and Prevention of Corrosion.* 2nd ed. Prentice Hall. Hoboken, NJ (1996).
10. Nonnenmacher, M., O'Boyle, M., Wickramasinghe, H. K. Kelvin probe force microscopy. *Applied Physics Letters.* **58** (25), 2921-2923 (1991).
11. Voigtländer, B. Work function, contact potential, and Kelvin probe AFM.*In Atomic Force Microscopy. NanoScience and Technology.* Springer. Cham (2019).
12. Melitz, W., Shen, J., Kummel, A. C., Lee, S. Kelvin probe force microscopy and its application. *Surface Science Reports.* **66** (1), 1-27 (2011).
13. Bagotsky, V. S. *Fundamentals of electrochemistry.* John Wiley & Sons, Inc., Hoboken, New Jersey (2006).
14. Bockris, J. O. M., Reddy, A. K. N., Gamboa-Aldeco, M. *Modern Electrochemistry 2A: Fundamentals of electrodics.* Kluwer Academic Publishers (2002).
15. Schmutz, P., Frankel, G. S. Characterization of AA2024-T3 by scanning Kelvin probe force microscopy. *Journal of the Electrochemical Society.* **145** (7), 2285-2295 (1998).
16. Blucher, D. B., Svensson, J. E., Johansson, L. G., Rohwerder, M., Stratmann, M. Scanning Kelvin probe force microscopy - A useful tool for studying atmospheric

corrosion of MgAl alloys in situ. *Journal of the Electrochemical Society.* **151** (12), B621-B626 (2004).

17. Guillaumin, V., Schmutz, P., Frankel, G. S. Characterization of corrosion interfaces by the scanning Kelvin probe force microscopy technique. *Journal of the Electrochemical Society.* **148** (5), B163-B173 (2001).
18. Hurley, M. F. et al. Volta potentials measured by scanning Kelvin probe force microscopy as relevant to corrosion of magnesium alloys. *Corrosion.* **71** (2), 160-170 (2015).
19. Jonsson, M., Thierry, D., LeBozec, N. The influence of microstructure on the corrosion behaviour of AZ91D studied by scanning Kelvin probe force microscopy and scanning Kelvin probe. *Corrosion Science.* **48** (5), 1193-1208 (2006).
20. Örnek, C., Engelberg, D. L. Correlative EBSD and SKPFM characterisation of microstructure development to assist determination of corrosion propensity in grade 2205 duplex stainless steel. *Journal of Materials Science.* **51** (4), 1931-1948 (2016).
21. Rohwerder, M., Hornung, E., Stratmann, M. Microscopic aspects of electrochemical delamination: An SKPFM study. *Electrochimica Acta.* **48** (9), 1235-1243 (2003).
22. Schmutz, P., Frankel, G. S. Corrosion study of AA2024-T3 by scanning Kelvin probe force microscopy and in situ atomic force microscopy scratching. *Journal of the Electrochemical Society.* **145** (7), 2295-2306 (1998).
23. Örnek, C., Leygraf, C., Pan, J. On the Volta potential measured by SKPFM - Fundamental and practical aspects with relevance to corrosion science. *Corrosion Engineering, Science and Technology.* **54** (3), 185-198 (2019).
24. Cook, A. B. et al. Calibration of the scanning Kelvin probe force microscope under controlled environmental conditions. *Electrochimica Acta.* **66**, 100-105 (2012).
25. Efaw, C. M. et al. Toward improving ambient Volta potential measurements with SKPFM for corrosion studies. *Journal of the Electrochemical Society.* **166** (11), C3018-C3027, (2019).
26. Örnek, C., Leygraf, C., Pan, J. Passive film characterisation of duplex stainless steel using scanning Kelvin probe force microscopy in combination with electrochemical measurements. *npj Materials Degradation.* **3** (1), 8 (2019).
27. Rohwerder, M., Turcu, F. High-resolution Kelvin probe microscopy in corrosion science: Scanning Kelvin probe force microscopy (SKPFM) versus classical scanning Kelvin probe (SKP). *Electrochimica Acta.* **53** (2), 290-299 (2007).
28. Mallinson, C. F., Watts, J. F. Communication-The effect of hydrocarbon contamination on the Volta potential of second phase particles in beryllium. *Journal of the Electrochemical Society.* **163** (8), C420-C422 (2016).
29. Liu, R. L. et al. Controlling the corrosion and cathodic activation of magnesium via microalloying additions of Ge. *Scientific Reports.* **6**, 28747 (2016).
30. Kvryan, A. et al. Microgalvanic corrosion behavior of Cu-Ag active braze alloys investigated with SKPFM. *Metals.* **6**, 91-107 (2016).
31. Davis, P. H. et al. Phase separation in Ti-6Al-4V alloys with boron additions for biomedical applications: Scanning Kelvin probe force microscopy investigation of microgalvanic couples and corrosion initiation. *JOM.* **69** (8), 1446-1454 (2017).

32. Benzing, J. T. et al. Impact of grain orientation and phase on Volta potential differences in an additively-manufactured titanium alloy. *AIP Advances.* **11** (2), 025219 (2021).
33. Baker, H., Avedesian, M. M. *Magnesium and Magnesium Alloys ASM Specialty Handbook.* ASM International. Materials Park, OH (1999).
34. Polmear, I. J., Nie, J.-F., Qian, M., StJohn, D. *Light Alloys: Metallurgy of the Light Metals.* Butterworth-Heinemann. Oxford, UK (2017).
35. Saha, P. et al. Rechargeable magnesium battery: Current status and key challenges for the future. *Progress in Materials Science.* **66**, 1-86 (2014).
36. Jacobson, D. M., Humpston, G. *Principles of Brazing.* ASM International. Materials Park, OH (2005).
37. Paiva, O. C., Barbosa, M. A. Microstructure, mechanical properties and chemical degradation of brazed AISI 316 stainless steel/alumina systems. *Materials Science and Engineering: A.* **480** (1-2), 306-315 (2008).
38. Kozlova, O., Voytovych, R., Devismes, M. F., Eustathopoulos, N. Wetting and brazing of stainless steels by copper-silver eutectic. *Materials Science and Engineering: A.* **495** (1-2), 96-101 (2008).
39. Boyer, R. R. An overview on the use of titanium in the aerospace industry. *Materials Science and Engineering: A.* **213** (1), 103-114 (1996).
40. Gurrappa, I. Characterization of titanium alloy Ti-6Al-4V for chemical, marine and industrial applications. *Materials Characterization.* **51** (2), 131-139 (2003).
41. Leyens, C., Peters, M. *Titanium and Titanium Alloys: Fundamentals and Applications.* John Wiley & Sons. Hoboken, NJ (2003).
42. Elias, C. N., Lima, J. H. C., Valiev, R., Meyers, M. A. Biomedical applications of titanium and its alloys. *JOM.* **60** (3), 46-49 (2008).
43. Mohammed, M. T., Khan, Z. A., Siddiquee, A. N. Beta titanium alloys: The lowest elastic modulus for biomedical applications: A review. *International Journal of Chemical, Molecular, Nuclear, Materials and Metallurgical Engineering.* **8** (8), 821-827 (2014).
44. Oezcan, M., Haemmerle, C. Titanium as a reconstruction and implant material in dentistry: Advantages and pitfalls. *Materials.* **5** (9), 1528-1545 (2012).
45. Tan, X. et al. Graded microstructure and mechanical properties of additive manufactured Ti-6Al-4V via electron beam melting. *Acta Materialia.* **97**, 1-16, (2015).
46. Cox, B. Pellet-clad interaction (PCI) failures of zirconium alloy fuel cladding - A review. *Journal of Nuclear Materials.* **172** (3), 249-292 (1990).
47. Efaw, C. M. et al. Characterization of zirconium oxides part II: New insights on the growth of zirconia revealed through complementary high-resolution mapping techniques. *Corrosion Science.* **167**, 108491 (2020).
48. Castanon, E. G. et al. Calibrated Kelvin-probe force microscopy of 2D materials using Pt-coated probes. *Journal of Physics Communications.* **4** (9), 095025 (2020).